

Combinatorial synthesis and rapid characterization of $\text{Mo}_{1-x}\text{Sn}_x$ ($0 \leq x \leq 1$) thin films

A. Bonakdarpour, K.C. Hewitt, T.D. Hatchard, M.D. Fleischauer, J.R. Dahn*

Department of Physics, Dalhousie University, Halifax, NS, Canada B3H 3J5

Received 19 July 2002; received in revised form 15 April 2003; accepted 23 April 2003

Abstract

Thin films of $\text{Mo}_{1-x}\text{Sn}_x$, continuously and linearly mapped for $0 < x < 1$, have been prepared by d.c. magnetron sputter deposition under various growth conditions. X-ray diffraction results indicate that as x in high-pressure deposited $\text{Mo}_{1-x}\text{Sn}_x$ increases from 0 to approximately 0.45, the bcc lattice expands and no new phases are formed. At low deposition pressures, Mo_3Sn , a β -tungsten structured phase, is formed along with the bcc Mo–Sn solid solution for $0.1 < x < 0.3$. The variation of the lattice parameter for this intermetallic phase also indicates that solid solutions, possibly of the form Mo_{3+y}Sn , are being formed. These materials are of special interest as anode candidates in lithium-ion batteries.

© 2003 Elsevier Science B.V. All rights reserved.

Keywords: Combinatorial synthesis; Mo–Sn films; Bcc and β -tungsten phases

1. Introduction

In the past few years, there has been a growing interest in combinatorial methods for synthesizing and characterizing solids. These methods refer to the simultaneous synthesis of hundreds or thousands of distinct materials by employing common deposition techniques such as magnetron sputtering. Combinatorial synthesis followed by rapid characterization enables materials scientists to rapidly map the structure–property relationships of potential systems and to efficiently identify optimized compositions [1]. Using these methods, new high temperature superconductors, magnetoresistors, phosphors and fuel cell catalysts have been reported [2–5]. Using combinatorial synthesis, both discrete and continuous compositions can be fabricated. Xiang and co-workers have developed both of these techniques using computer-controlled masking of the sputtered atoms [6,7]. van Dover has shown continuous mapping, using composition spread techniques, in the discovery of new dielectrics and magnetic materials [8].

Recently, we have developed a continuous combinatorial sputtering method using appropriately designed

masks. So far, we have successfully applied it to several binary and ternary systems in pursuit of new anode materials for lithium-ion batteries. The methodology is simple, robust, and allows for linear, constant or other desired functional form gradients in the composition. More details about our combinatorial approaches can be found elsewhere [9].

In the past few years, there has been extensive research on metals that alloy with lithium (e.g. Sn) for use in rechargeable lithium batteries. Up to 4.4 lithium atoms can be alloyed with tin. Upon alloying/de-alloying with lithium, however, alloy grains crack due to inhomogeneous expansion and contraction. This mechanical failure limits the lifetime of the battery to only a few cycles. Yang et al. suggested that grain fragmentation can be minimized if the active alloying component can be contained in an inactive matrix [10]. For example, alloying/non-alloying $\text{Sn}_2\text{Fe}/\text{SnFe}_3\text{C}$ has been shown to have good cycling performance [11]. Previous promising work on sequentially-sputtered Mo–Sn films with fixed Mo–Sn compositions, initiated our efforts to prepare the whole range of Mo–Sn materials by combinatorial methods and study their structural and electrochemical properties [12]. Here, synthesis and structural properties of $\text{Mo}_{1-x}\text{Sn}_x$ films will be present-

*Corresponding author. Tel.: +1-902-494-2312; fax: +1-902-494-5191.

E-mail address: jeff.dahn@dal.ca (J.R. Dahn).

ed. The electrochemical studies of these Mo–Sn films will be reported elsewhere.

2. Experimental methods

The composition range $0 < x < x_{\max}$ in $\text{Mo}_{1-x}\text{Sn}_x$ was produced in a single sputter deposition by a Corona Vacuum Coater's V3T sputtering system. The system is equipped with a 500 l/s turbo pump and a R2000 series Polycold fast cycle water-vapor cryopump to achieve a base pressure of approximately 1×10^{-7} Torr. The substrate was plasma-cleaned for 20 min under O_2 (20 mTorr) and 10 min under Ar (10 mTorr) plasma to ensure good adhesion. Two-inch 99.9% pure Mo and Sn targets (Kurt J. Lesker) were sputtered by DC power sources (Advanced Energy MDX-1K) onto copper foil for microprobe analysis and onto glass microscope slides for X-ray diffraction studies. The sputtering parameters, including pressure, power, voltage and current for the different growth experiments are summarized in Table 1.

All but one growth was performed for $0 < x < 0.45 = x_{\max}$, because this range is of interest for the electrochemical studies. The linear variation of x in $\text{Mo}_{1-x}\text{Sn}_x$ was obtained by positioning constant and linear deposition masks [9] directly opposite the Mo and Sn targets. The functional forms of these mask slots are computed so as to convert the Gaussian-like shape of the sputtered atomic beams into constant and linear deposition profiles, while the substrate table is rotating during the growth (Fig. 1). Approximately 1 Å of Mo and Sn are deposited under each pass of the substrate table. The substrate table is approximately 6 cm away from the targets and is water-cooled during the run. Targets were pre-sputtered for approximately 2 min to remove surface oxides and impurities. A stable sputtering voltage is a good indication of a clean target surface.

X-ray diffraction patterns were taken point by point on the films using an Inel curved position sensitive detector (CPS 120) and a PW-1720 Philips X-ray generator using Cu $K\alpha$ radiation. The incident beam was set to be incident at 85° with respect to the surface normal. The system is equipped with an automated X–Y motion stage, which makes it an ideal tool for

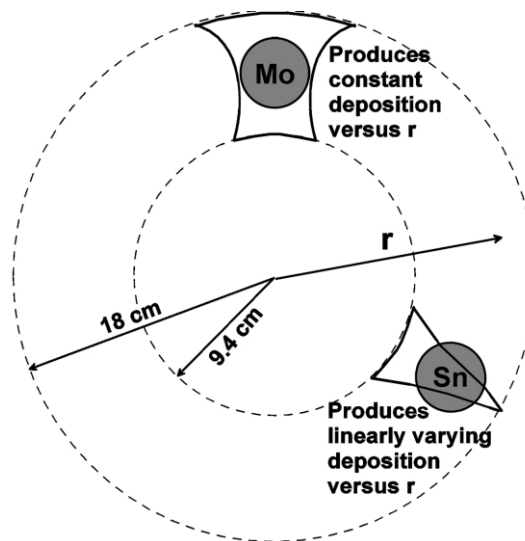


Fig. 1. Schematic representation of the masking setup used inside our sputtering chamber. Sputtering masks are used to deposit a linear range of Sn and a constant amount of Mo to produce the binary system, $\text{Mo}_{1-x}\text{Sn}_x$.

analyzing combinatorial samples. The X-ray reflections for the entire $5^\circ < 2\theta < 120^\circ$ range were detected simultaneously by the CPS for 0.032° increments. The Inel simulates a diffractometer with a fixed sample and tube and a rotating detector; thus, the direction of the scattering vector varies for different 2θ . The beam size is approximately 1 mm in width and is fixed.

Accurate, quantitative composition analysis of the samples was made using a JEOL JXA-8200 Superprobe equipped with one energy dispersive spectrometer (EDS), five wavelength dispersive spectrometers (WDS), and an automated motion stage. Metals content (Mo, Sn and Cu substrate) was measured by EDS and oxygen content was analyzed by WDS. The electron beam was maintained at 15 kV, 10 nA, and was 10 μm in diameter. The probe utilized a beam stabilizer and was optically focused before each measurement. The accuracy of these measurements is approximately 1%. Using these automated instruments, the structure and composition of the entire range of a binary system like $\text{Mo}_{1-x}\text{Sn}_x$ ($0 \leq x \leq 1$) could be determined rapidly.

Table 1
Summary of Mo–Sn sputtering experiments

Growth ID	Flow rate (sccm)	Argon pressure (mTorr)	Sn (P/V/I) (W/V/A)	Mo (P/V/I) (W/V/A)	Time (h)	Rotation speed (rpm)
SPD90	2.0	3.3	25/306/0.08	75/304/0.24	4.0	
SPD99	8.5	10	25/274/0.09	75/255/0.30	5.8	23
SPD103	1.0	1.8	25/378/0.23	75/323/0.23	6.0	23
SPE1	4.0	5.0	25/315/0.076	75/287/0.253	5.0	17
SPE5	0.6	1.5	28/339/0.08	75/315/0.231	9.0	17
SPE21	0.6	1.4	28/313/0.085	75/295/0.247	9.0	17

Structure refinements of X-ray data were made using Hill and Howard's version of the Rietveld program RIETICA, using space groups Im3m and Pm-3n for the bcc and Mo₃Sn phases, respectively [13,14]. The Mo₃Sn structure is the same as that of β -tungsten, with Sn in 2a sites and Mo in 6c sites [15]. When the two phases co-existed, both were refined simultaneously. The Bragg-*R* factor for all the refinements was approximately 5 or less, for both phases. Since a large number of X-ray patterns were collected, one for every $\Delta x \sim 0.02$, we were able to follow the structural changes very precisely.

Copper foil discs, 15 μm thick, 1.3 cm diameter were weighed before and after the deposition using a Cahn 29 microbalance. An approximate measure of the film thickness was determined using an approximate density of $\rho(x) = (1-x)\rho_{\text{Mo}} + x\rho_{\text{Sn}}$ and the nominal densities of $\rho_{\text{Mo}} = 10.2 \text{ g/cm}^3$ and $\rho_{\text{Sn}} = 7.3 \text{ g/cm}^3$. This is only an approximation because densities vary with sputtering pressure.

3. Results and discussion

3.1. Crystallographic phases

According to the empirical Hume–Rothery rules for substitutional solid solutions, there should not be much solubility in the Mo–Sn binary system [16]. Elemental Mo and Sn fail two requirements of the above, namely having similar crystal structure and possessing the same stable oxidation states. Mo crystallizes in a bcc structure and its most stable oxidation state is 6⁺, whereas Sn has a tetragonal structure with oxidation states of 4⁺ and 2⁺. Indeed, the Mo–Sn system has shown no equilibrium miscibility [17]. In addition to our recent report on bcc Mo–Sn films, three metastable intermetallic phases, Mo₃Sn, Mo₂Sn₃ and MoSn₂ have been reported in the literature. Killpatrick prepared the metastable Mo₃Sn phase using high-pressure (35 kbar), high-temperature (1000 °C) annealing, followed by a rapid quench to 100 °C in 20 s [18]. The compound had a β -tungsten structure with a lattice parameter of 5.094 Å (Fig. 2) and was always obtained with an alloy Mo–Sn phase. Reports on the other phases were never published. Only in a note added in proof in a paper on As and Ge compounds, Brown mentions that he prepared three Mo–Sn compounds [19].

Table 2 summarizes the different combinatorial Mo–Sn samples made. Sample SPD103, made with $0 < x < 0.92$ in Mo_{1-x}Sn_x, spanned approximately the entire range of the Mo–Sn binary phase diagram. The sample was sputtered at low pressure (1.8 mTorr). Fig. 3 shows the results of electron microprobe analysis of this sample demonstrating that the desired linear composition variation has been obtained. Fig. 4 shows some of the X-ray patterns of this combinatorial sample. Various phases make up the film. Fig. 4 shows regions of crystalline

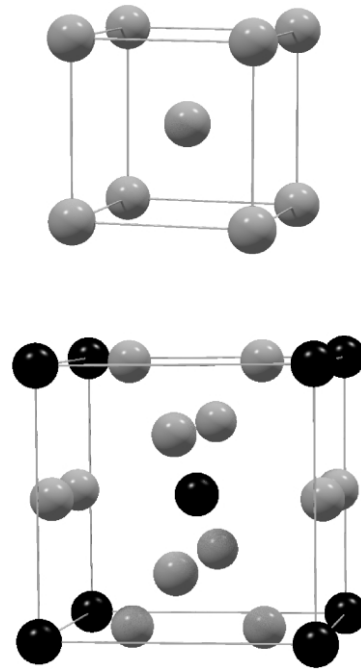


Fig. 2. Unit cells of bcc Mo (a) and β -tungsten structure Mo₃Sn (b). Dark spheres represent Sn atoms.

Sn, nanocrystalline Sn coexisting with nanocrystalline Mo_{0.53}Sn_{0.37}, crystalline bcc Mo_{1-x}Sn_x for $0 < x < 0.37$ and crystalline Mo₃Sn type for $0.1 < x < 0.32$.

Above $x = 0.36$ the bcc peaks become very broad indicating the formation of nano-sized grains, presumably because the solubility limit of the bcc phase has been reached and long-range crystal order is disturbed by nano-sized tin grains [12]. This solubility limit apparently depends on the sputtering conditions. In a higher-sputter-pressure sample, SPE1, up to 46% Sn solubility is observed. In the range of $0.1 < x < 0.3$ in Mo_{1-x}Sn_x, the Mo₃Sn phase co-exists with the bcc phase. X-ray peaks of the Mo₃Sn phase attain a maximum intensity at approximately $x = 0.2$ as shown in Fig. 5. The region of the film where the Mo₃Sn phase is found appears as a diffuse reflecting band in an otherwise shiny and reflective film.

Fig. 6 shows some of the X-ray diffraction patterns collected for sample SPE1, deposited at high pressure. Compared to Fig. 5, very little Mo₃Sn phase is observed in any pattern. Only when $x \sim 0.2$ weak peaks from the Mo₃Sn phase are observed. The results in Figs. 4–6 suggest that the Mo₃Sn phase forms predominantly at low sputtering pressure. In sputter deposition, the energy of the ejected particles (target atoms or neutrals) is known to drop exponentially as a function of the pressure–distance variable as $E = E_0 \exp^{-cpd}$, where E_0 is the energy of ejected particles at the target surface, p is the argon pressure, d is the target–substrate distance, and c is a characteristic constant for the ejected species

Table 2
Summary of the observations of the Mo–Sn sputtered films

ID	x in $\text{Mo}_{1-x}\text{Sn}_x$	y in $[\text{MoSn}]_{1-y}\text{O}_y$	Thickness t (μm)	Structure and phases
SPD90	$0.05 < x < 0.42$	~ 0.15		Crystalline bcc for $x < 0.40$ sharp 1 1 0 peaks and 1 1 2 orientation mixture of Mo_3Sn for $0.1 < x < 0.34$
SPD99	$0.02 < x < 0.36$	~ 0.4	$0.04 < t < 0.85$	Broad bcc peaks small texturing, 'powder-like' pattern
SPD103	$0.05 < x < 0.92$	~ 0.1		Crystalline Sn for $x \sim 0.91$ nano-sized bcc($\text{Mo}_{0.63}\text{Sn}_{0.37}$) and Sn for $0.37 < x < 0.9$ nano-sized and crystalline bcc for $x \sim 0.34$ bcc $\text{Mo}_{1-x}\text{Sn}_x$ and Mo_3Sn -type for $0.1 < x < 0.33$ bcc phase below $x = 0.1$
SPE1	$0.05 < x < 0.46$	$\sim 0.25 \pm 0.05$	$0.50 < t < 1.2$	'Powder-like' pattern for $0.4 < x < 0.45$ For $x < 0.4$, (1 1 0) and (1 1 2) peaks of bcc dominate broad bcc peaks for all x
SPE5	$0.02 < x < 0.50$	None for $0.3 < x < 0.5$ –0.10 for $x < 0.3$	$0.7 < t < 1.64$	Nano-sized bcc for $x \sim 0.36$, crystalline bcc for $x < 0.36$ bcc and Mo_3Sn mixture for $0.11 < x < 0.31$ maximum Mo_3Sn -type phase seen for $x \sim 0.18$ (2 0 0) orientation of bcc grows and declines for $0.10 < x < 0.33$ (2 0 0) orientation of bcc peaks for $x \sim 0.23$ bcc for $x < 0.11$
SPE21	$0.03 < x < 0.5$	None for $x > 0.25$ –0.06 for $x > 0.25$	$0.75 < t < 1.9$	Nano-sized bcc for $x > 0.40$, crystalline bcc for $x < 0.40$ Bcc and Mo_3Sn for $0.10 < x < 0.33$ Bcc for $x < 0.10$ (2 0 0) orientation of bcc intensifies and diminishes for $0.10 < x < 0.33$ (2 0 0) orientation of the bcc phase peaks for $x \sim 0.25$

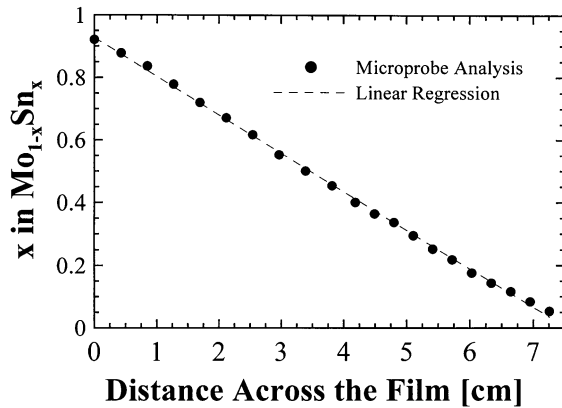


Fig. 3. The linear composition grading of $\text{Mo}_{1-x}\text{Sn}_x$ (SPD103) across the film for $0 < x < 1$.

[20,21]. We believe that low sputtering pressures simulate the conditions of high-pressure, high-temperature formation of the Mo_3Sn phase reported in Ref. [18]. It might be possible to obtain single phase Mo_3Sn by tuning the sputtering conditions, however, we have always observed a mixture of the two phases even with a low sputtering pressure of 1.3 mTorr.

Fig. 7 shows the Rietveld profile refinement to a selected X-ray diffraction pattern taken from sample SPD103 at a composition $x=0.2$ in $\text{Mo}_{1-x}\text{Sn}_x$. Both the bcc and Mo_3Sn phases were included in the refinement. Because the films exhibit texture, a provision for preferred orientation was made in the refinement in order to get acceptable fits. It was our main goal to refine all the patterns in order to extract the lattice constant variation with x for both phases, and we were able to do this reliably. Fig. 8a and b show the lattice constant variation for the bcc and Mo_3Sn phases plotted vs. x in $\text{Mo}_{1-x}\text{Sn}_x$.

The linear variation in the lattice constant of both the bcc- and Mo_3Sn -type phases suggests that solid solutions with a wide compositional range are being formed. Addition of Sn atoms with a metallic radius of 1.58 Å expands the bcc lattice of Mo (metallic radius = 1.40 Å) in a linear manner, according to Vegard's law. Fig. 8a shows that at $x=0.36$, a sudden increase in the bcc lattice size is observed. This also corresponds to a transition from sharp crystalline peaks to broad nanophase peaks (Fig. 4).

Fig. 8b shows that the Mo_3Sn phase also shows a linear variation in its lattice constant. If a lattice constant of 5.09 Å corresponds to stoichiometric Mo_3Sn in our film, then the Mo_3Sn solid solution could contain extra Mo as Mo_{3+y}Sn , resulting in a lattice contraction, as observed. This is the first report of Mo_3Sn having a wide stoichiometry range. We believe that the high quenching rates inherent in the sputtering process allow this metastable phase to be quenched in over a wide

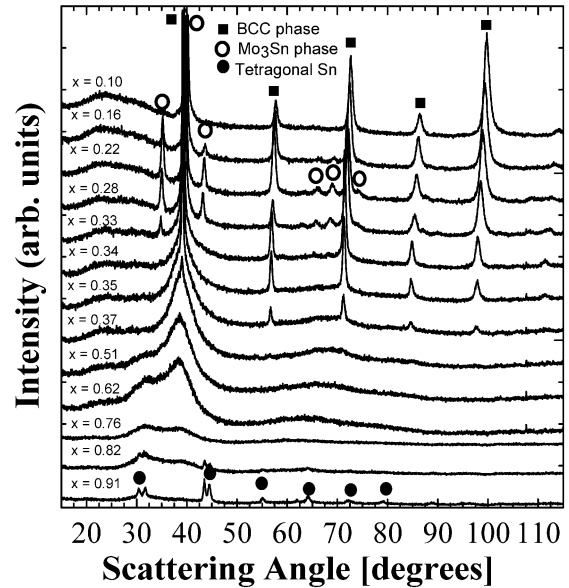


Fig. 4. X-ray diffraction profiles of $\text{Mo}_{1-x}\text{Sn}_x$ (SPD103) for a selected number of compositions. Open circles, solid squares and solid circles indicate Mo_3Sn -type, bcc Mo_{1-x}Sn and crystalline Sn, respectively. The uncertainty in values of x is approximately ± 0.02 . (Note: the first three diffractograms were obtained in shorter periods. The structural changes occur smoothly. Here, only 13 out of 50 collected patterns are shown.)

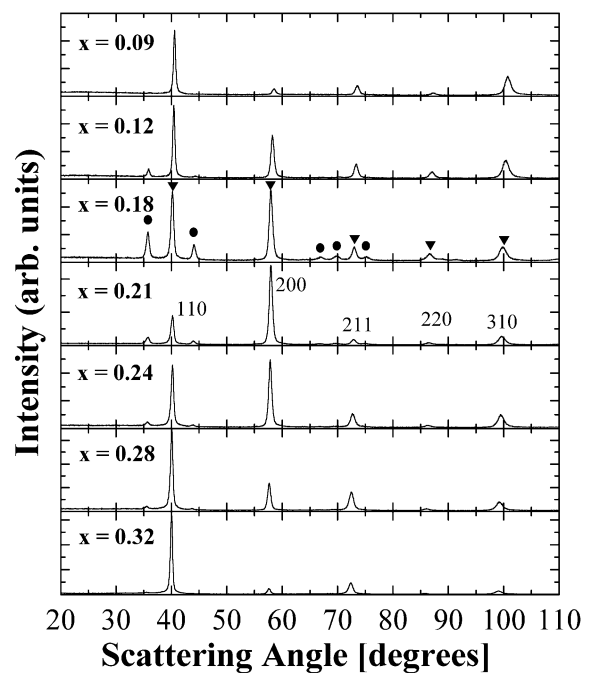


Fig. 5. The appearance and disappearance of the Mo_3Sn phase (SPE21). Notice a dramatic texture turnover in the bcc phase: (2 0 0) planes are highly favored just before a maximum in the Mo_3Sn phase is observed, and they recede as Mo_3Sn diminishes. Solid triangles and circles mark the bcc and Mo_3Sn -type phase, respectively. The Miller indices of the bcc phase are indicated.

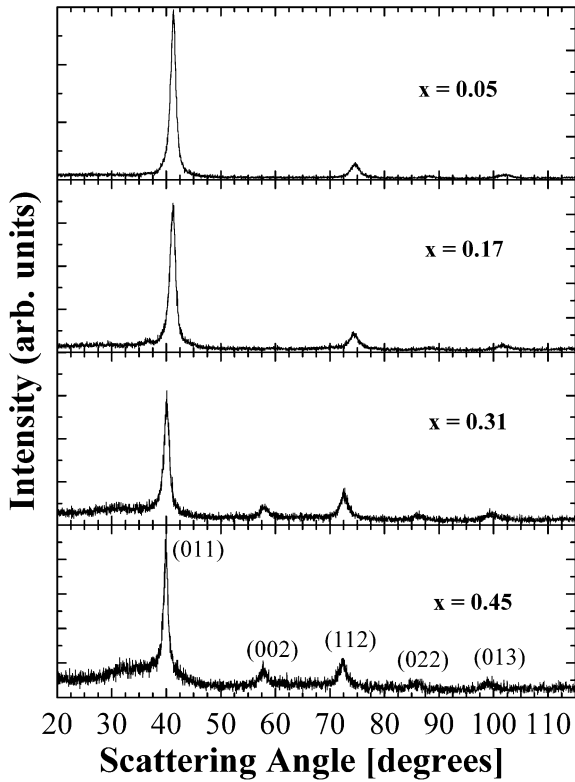


Fig. 6. Broad bcc peaks of SPE1 for $0 < x < 0.45$, grown at 5 mTorr. Very little Mo_3Sn is seen. The compositions, x , are indicated in the figure. As x increases, (1 1 2) texturing increases. At $x=0.45$, Sn begins to precipitate out.

composition range. Klabunde et al. have observed Mo_3Si , which is isostructural with Mo_3Sn , in Mo films sputtered on silica substrates. They report that the formation of Mo_3Si is well known for Mo deposited onto silicon substrates [22]. We have not observed any Mo_3Si for either Mo–Sn or pure Mo sputtered on glass slides.

At higher sputtering pressures, we observe predominantly single phase bcc $\text{Mo}_{1-x}\text{Sn}_x$. Fig. 6 shows selected X-ray diffractograms of $\text{Mo}_{1-x}\text{Sn}_x$ grown at 5 mTorr (SPE1) for $x=0$ –46%. The peaks are broader than the low-pressure deposited $\text{Mo}_{1-x}\text{Sn}_x$, indicating smaller grain size. The bcc phase exists up to $x=0.46$. A similar effect of argon pressure on the grain size of sputtered Mo has been reported before [22]. Fig. 9 shows the variation of the lattice parameter with composition for this combinatorial sample. It agrees well with the trend seen in Fig. 8a. Over this compositional range, bcc $\text{Mo}_{1-x}\text{Sn}_x$ obeys Vegard's law and exists as a solid solution.

3.2. Oxygen content

Fig. 10 shows the variation of the oxygen content of low- (SPE21) and high-pressure (SPE1) sputtered sam-

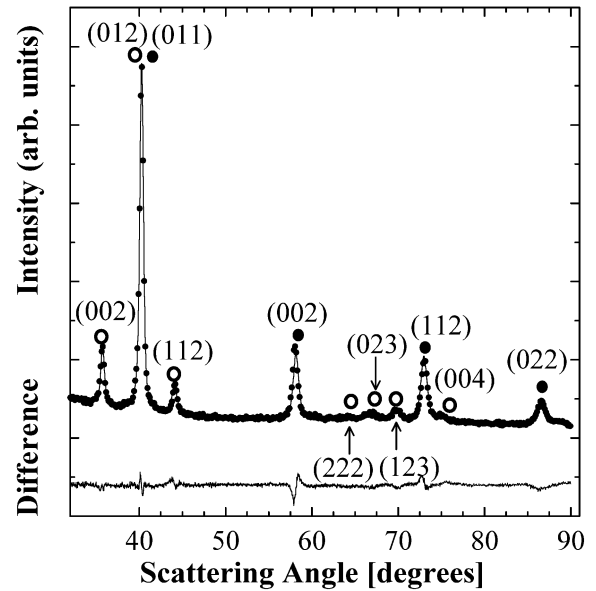


Fig. 7. The X-ray diffraction profiles of $\text{Mo}_{0.8}\text{Sn}_{0.2}$ for mixed bcc and β -tungsten type Mo_3Sn phases and the corresponding two-phase Rietveld refinement. Open and filled circles mark the Mo_3Sn and the bcc phase, respectively. The difference between experiment and calculation is shown as the dashed line below. The (0 1 1) peak of the bcc phase and the (0 1 2) peak of the Mo_3Sn -type phase cannot be resolved. The Bragg- R factors of the refinements were 2.9 and 2.3 for the bcc and Mo_3Sn phase, respectively.

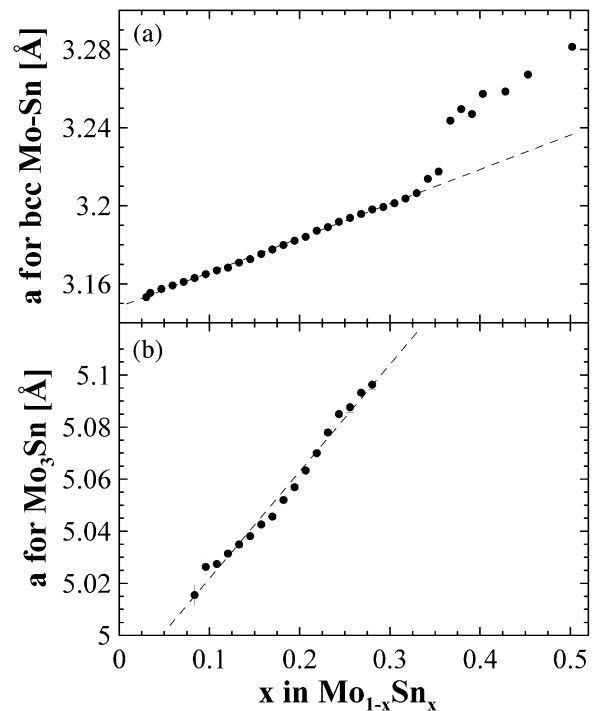


Fig. 8. Variation of the cubic lattice parameter of the (a) bcc $\text{Mo}_{1-x}\text{Sn}_x$ phase and (b) the Mo_3Sn -type phase vs. x for sample SPD103.

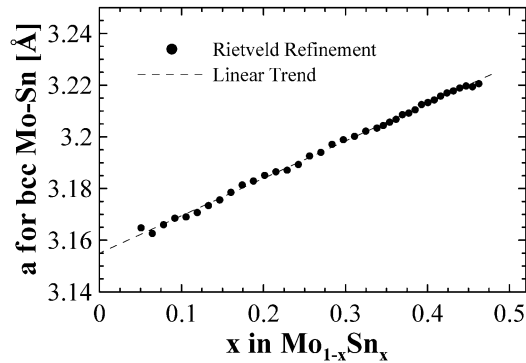


Fig. 9. Variation of the cubic lattice parameter of the bcc $\text{Mo}_{1-x}\text{Sn}_x$ phase vs. x for sample SPE1.

ples as a function of position on the films. The low-pressure deposited film shows a minimal amount of oxygen in contrast to the high-pressure film. Klabunde et al. attribute the oxygen content of high-pressure sputtered Mo films to their porous microstructure [22]. They have shown that high-pressure-deposited Mo films have much lower densities and contain columnar voids that are susceptible to post-deposition oxidation. Our results are consistent with their observations.

3.3. Diagram of phases observed in the composition-sputtering pressure plane

Fig. 11 shows a diagram of the phases observed in the sputtered films as a function of both x in

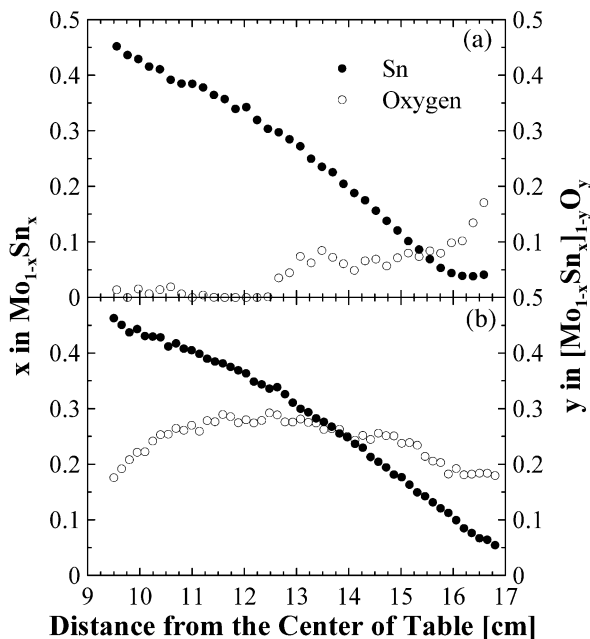


Fig. 10. Positional variations of Sn (x in $\text{Mo}_{1-x}\text{Sn}_x$) and oxygen (y in $[\text{Mo}_{1-x}\text{Sn}_x]_{1-y}\text{O}_y$) across the film for 1.4 mTorr (a) (SPE21) and for 5.0 mTorr (b) Ar pressure (SPE1).

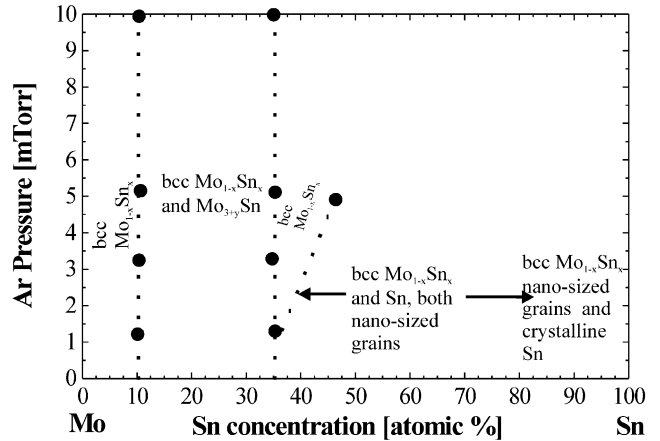


Fig. 11. Diagram of the observed phases as a function of x in $\text{Mo}_{1-x}\text{Sn}_x$ and sputtering pressure. The Mo_3Sn -type and bcc phases co-exist for $0.1 < x < 0.3$ in the pressure range shown, however, as the pressure increases, the amount of the Mo_3Sn phase decreases. At 10 mTorr, the strongest Mo_3Sn peak (0 0 2) is barely visible. Samples for $0.5 < x < 1.0$ were only studied at 1.8 mTorr.

$\text{Mo}_{1-x}\text{Sn}_x$ and argon pressure during sputtering. The most notable effects of increased pressure are the reduction of the amount of the Mo_3Sn -type phase and the extension of the stability range of the bcc $\text{Mo}_{1-x}\text{Sn}_x$ phase. The phase diagram presents the data on phases deposited onto a 15 °C substrate table. The impact of post-annealing treatment on Mo–Sn films have been reported before [12].

4. Conclusions

The power of combinatorial techniques in synthesis of materials is clearly shown in this instance for Mo–Sn films. The entire stoichiometry range was obtained in a single sputtering run, and smooth transitions from various regions of crystalline and nano-crystalline phases are observed. Sputtering promotes formation of solid solutions of bcc $\text{Mo}_{1-x}\text{Sn}_x$ and β -tungsten structure Mo_{3+y}Sn , neither of which can be prepared by equilibrium methods. The effect of sputtering pressure on the phases formed was described. The dependence of the oxygen content of the sputtered films as a function of composition and sputtering pressure was investigated.

Acknowledgments

The authors acknowledge NSERC and 3M Canada for the funding of this work. Furthermore, T.H. and M.F. acknowledge NSERC for scholarship support.

References

- [1] E.J. Amis, X.D. Xiang, J.C. Zhao, MRS Bull. 27 (2002) 295.
- [2] X.D. Xiang, X. Sun, G. Briceno, Y. Lou, K.A. Wang, H.Y. Chang, W.G. Wallace-Freedman, S.W. Chen, P.G. Schultz, Science 268 (1995) 1738.

- [3] G. Briceno, H. Chang, X. Sun, P.G. Schultz, X.D. Xiang, *Science* 270 (1995) 273.
- [4] J. Wang, K. Yoo, C. Gao, I. Takeuchi, X. Sun, H. Chang, X.D. Xiang, *Science* 279 (1998) 1712.
- [5] E. Reddington, A. Sapienza, B. Gurau, R. Viswanathan, S. Sarangapani, E.S. Smotkin, T.E. Mallouk, *Science* 280 (1998) 1735.
- [6] X.D. Xiang, *Mater. Sci. Eng. B—Solid* 56 (1998) 246.
- [7] Y.K. Yoo, T. Ohnishi, G. Wang, F. Duerwer, X.D. Xiang, Y.S. Chu, D.C. Mancini, Y.Q. Li, R.C. O’Handley, *Intermetallics* 9 (2001) 541.
- [8] R.B. van Dover, L.F. Schneemeyer, R.M. Fleming, *Nature* 392 (1998) 162.
- [9] J.R. Dahn, S. Trussler, T.D. Hatchard, A. Bonakdarpour, J.N. Mueller-Neuhaus, K.C. Hewitt, M. Fleischauer, *Chem. Mater.* 14 (8) (2002) 3519–3523.
- [10] J. Yang, M. Winter, J.O. Besenhard, *Solid State Ionics* 90 (1996) 281.
- [11] O. Mao, R.L. Turner, I.A. Courtney, B.D. Fredericksen, M.I. Buckett, L.J. Krause, J.R. Dahn, *Electrochem. Soc. Lett.* 2 (1999) 3.
- [12] J.R. Dahn, R.L. Turner, O. Mao, R.A. Dunlap, A.E. George, M.M. Buckett, D.J. McClure, L.J. Krause, *Thin Solid Films* 408 (2002) 111.
- [13] RIETICA v1.7.7, Microsoft Windows version of LHPM, R.J. Hill, C.J. Howard, *J. Appl. Crystallogr.* 18 (1985) 173.
- [14] D.B. Wiles, R.A. Young, *J. Appl. Crystallogr.* 14 (1981) 149.
- [15] P. Villars, L.D. Calvert, *Pearson’s Handbook of Crystallographic Data for Intermetallic Phases*, vol. 4, The Materials Information Society, Materials Park, OH, 1996.
- [16] G.F. Carter, D.E. Paul, *Materials Science and Engineering*, ASM International, 1991.
- [17] W.G. Moffatt, *The Handbook of Binary Phase Diagrams*, Genium Publishing Co, Schenectady, NY, 1990.
- [18] D.H. Killpatrick, *J. Phys. Chem. Solids* 25 (1965) 1499.
- [19] A. Brown, *Nature* 206 (1965) 502.
- [20] T.P. Drüsedau, F. Klabunde, P. Veit, T. Hempel, *Phys. Stat. Sol. (a)* 161 (1997) 167.
- [21] R.E. Somekh, *J. Vac. Sci. Technol. A* 2 (1984) 1285.
- [22] F. Klabunde, M. Lohmann, J. Blasing, T.J. Drusedau, *J. Appl. Phys.* 80 (1996) 6266.